hep-ph/0402019
LC-PHSM-2003-100
LUNFD6/(NFFL-7219)2004

The Unintegrated Gluon Density in the Photon and Heavy Quark Production

M. Hansson, H. Jung and L. Jönsson
Department of Physics
Lund University, Lund, Sweden

Abstract

The production cross section of heavy quarks in real and virtual photon-photon collisions has been studied. The unintegrated gluon density in the photon was obtained using the full CCFM evolution equation for the first time. The gluon density was implemented in the Monte Carlo generator CASCADE, and cross sections for heavy quark production in e^+e^- collisions were calculated and compared to LEP data. Also, predictions for heavy quark cross sections in e^+e^- and $\gamma\gamma$ collisions at TESLA energies are given.

1 Introduction

The production of heavy flavour (b and c quarks) in $\gamma\gamma$ collisions has been studied at LEP [1, 2, 3, 4, 5, 6, 7, 8, 9, 10] for many years and will be an important field of study at TESLA [11, 12]. It has also been studied in proton-photon collisions at HERA [13, 14, 15, 16, 17, 18], and in proton-proton collisions at the TEVATRON [19, 20, 21, 22]. Whereas originally the measured charm cross sections were well described by the parton evolution according to the standard collinear approach, the measured beauty cross sections were a factor 2-4 larger than predictions. It has been shown [23, 24, 25] that an improved description of the heavy quark fragmentation function together with new parametrizations of structure functions and resumming next-to-leading logarithms in NLO QCD calculations result in an improved description of the B meson cross section in $p\bar{p}$ and e^+e^- collisions. Also the application of k_t-factorization and an unintegrated gluon density for the proton gives beauty cross sections which are in good agreement with data from $p\bar{p}$ collisions [26, 27]. The aim of this paper is to investigate if the $b\bar{b}$ cross section also can be explained in $\gamma\gamma$ collisions by using k_t- factorization and an unintegrated gluon density for the photon.

In a previous study [28], using k_t-factorization, the unintegrated gluon density in the photon was calculated using a simplified solution to the CCFM formalism [29, 30, 31, 32] proposed by [33]. As an alternative approach also a generalization of the GBW saturation model [34, 35] was used to obtain the unintegrated gluon density. In the present study we will use the complete CCFM evolution equations to determine the unintegrated gluon density in the photon and calculate the heavy quark cross section with help of the CASCADE Monte Carlo program.

2 The structure of the photon

It is well known that the proton not only consists of three valence quarks, but also of virtual gluons that hold the quarks together. These gluons can split up in quark-antiquark pairs, called sea quarks, which in turn can emit gluons, see Figure 1a. A photon colliding with a proton may therefore interact either with one of the valence quarks or with one of the sea quarks.

In analogy with the proton, a photon can be seen as a flux of (virtual) quarks and gluons. However, the photon does not consist of any valence quarks, and must first fluctuate into a virtual quark-antiquark pair which can emit gluons, see Figure 1b. When a photon interacts with a virtual quark in another photon, the former is said to resolve the latter. How much of the photon that is resolved depends on the resolving power (virtuality Q^2) of the photon. So, what a photon with a low Q^2 will resolve as a quark, a photon with a higher Q^2 might resolve as a quark and a gluon which is radiated by the quark, sharing the original quark momentum. A photon with a very high Q^2 may also resolve the soft gluon as having split up in a quark-antiquark pair. This means that the more we resolve the more quarks we see at smaller x, since each daughter particle must have less momentum than the mother. The density of quarks and gluons thus depends on Q^2, a phenomenon called scaling violation. For photons, this Q^2 dependence occurs already with the anomalous part of the splitting, i.e. the splitting of the photon into a quark-antiquark pair. The density of quarks and gluons is described by the density function $f_i(x, \mu^2)$ which is just the probability that a parton of type i (quark or gluon) is carrying a longitudinal momentum fraction x of the photon, at a scale $\mu^2 = Q^2$. The scale is generally denoted μ^2, since it does not always have to be the virtuality of the photon that sets the scale. The structure function of the photon can then be written as

$$F_2^\gamma(x, \mu^2) = x \sum_i e_i^2 f_i^\gamma(x, \mu^2)$$

where e_i is the electric charge of parton i and one sums over all quark flavours. Of course, the photons cannot interact with the gluons, since $e_{gluon} = 0$, and F_2^γ does not depend on the gluon structure function explicitly (in LO and NLO in the DIS factorization scheme [36]). However, since the quark density at small x is driven by the gluon density, it is possible to extract $f_{gluon}(x, \mu^2)$. In general, the cross section that a parton i from one photon will interact with a parton j from another photon and form the final state X is

$$\sigma = \sum_{i,j} \int \frac{dx_1}{x_1} \frac{dx_2}{x_2} \cdot f_i^\gamma(x_1, \mu^2) \cdot f_j^\gamma(x_2, \mu^2) \cdot \hat{\sigma}_{i+j \to X}(x_1, x_2, s) \tag{1}$$

where the parton densities f_i^γ and f_j^γ describe the probability of finding partons i and j with momentum fractions x_1 and x_2 and the partonic cross section $\hat{\sigma}$ describes the probability

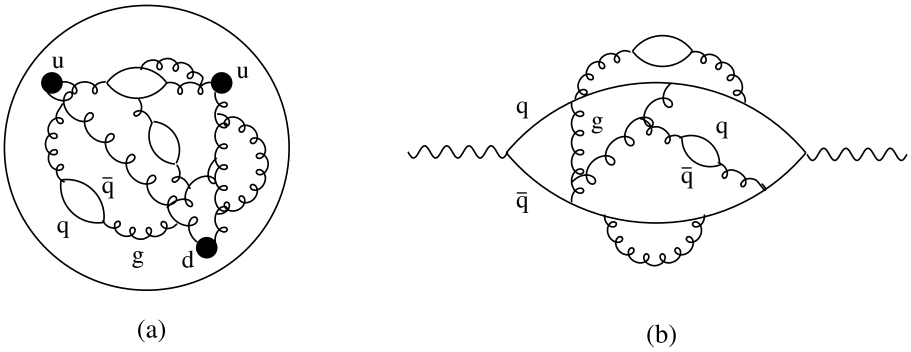

Figure 1: *The structure of the proton (a) and the photon (b).*

that the two particles i and j will create the final state X. The partonic cross section is proportional to the square of a Matrix Element (ME), which in turn depends on the masses, virtualities, couplings etc. of the particles involved. The integral is over all x_1 and x_2 allowed by the kinematics. Unlike the partonic cross section, the parton densities cannot be calculated from first principles. Instead, experimental fits and phenomenological methods must be used in order to describe the parton distributions inside the photon.

3 k_t-factorization

All factors in equation (1) above only depend on the longitudinal momentum fraction x and the scale μ^2. This means that all partons are assumed to travel in the same direction as the incoming particle, i.e. they have no transverse momenta. It is therefore called a collinear approximation. However, at large energies, where small x gluons are probed, the transverse momenta k_t of the partons are expected to be important. Therefore, the cross sections are factorized [37, 38, 39, 40] into a k_t-dependent partonic cross section $\hat{\sigma}(x, k_t^2, \mu^2)$, where the incoming partons are treated off-mass shell, and a k_t-dependent parton density function $\mathcal{A}(x, k_t^2, \mu^2)$. The equivalent to equation (1) then becomes

$$\sigma = \sum_{i,j} \int \frac{dx_1}{x_1} \frac{dx_2}{x_2} dk_{t1}^2 dk_{t2}^2 \mathcal{A}_i^\gamma(x_1, k_{t1}^2, \mu^2) \mathcal{A}_j^\gamma(x_2, k_{t2}^2, \mu^2) \hat{\sigma}_{i+j\to X}(k_{t1}, k_{t2}, x_1, x_2, s). \quad (2)$$

The function $\mathcal{A}(x, k_t^2, \mu^2)$ is called the (k_t-) unintegrated gluon density and is related to the collinear one by

$$g(x, \mu^2) \simeq \int_0^{\mu^2} dk_t^2 \mathcal{A}(x, k_t^2, \mu^2), \quad (3)$$

where $\mathcal{A}(x, k_t^2, \mu^2)$ describes the probability to find a gluon with a longitudinal momentum fraction x and a transverse momentum k_t at a scale μ^2. Inverting the relation (3) gives that an unintegrated gluon density may be obtained by differentiating an integrated gluon density with respect to μ^2,

$$\mathcal{G}(x, k_t^2) \equiv \left. \frac{dg(x, \mu^2)}{d\mu^2} \right|_{\mu^2 = k_t^2}. \quad (4)$$

Note that the unintegrated gluon density obtained in this way only depends on one scale, since $\mu^2 = k_t^2$. To distinguish the different parton distributions, the notation following [41] is used: $g(x, \mu^2)$ is the parton distribution in the collinear approach, while $\mathcal{G}(x, k_t^2)$ and $\mathcal{A}(x, k_t^2, \mu^2)$ are the one- and two-scale distributions in the k_t-factorization approach. When using off-shell matrix elements of leading order ($O(\alpha_s)$), some next-to leading order ($O(\alpha_s^2)$) processes in the collinear approach are effectively included, in addition to all collinear leading order processes.

4 Heavy quark production processes

Heavy quark production in photon collisions can be explained by three mechanisms, shown in Figure 2. At small $\sqrt{s}$, the cross section is dominated by the direct part (a-c). In this case, the photons couple directly to the quarks, and the process is therefore not dependent on the quark and gluon content in the photon. Hence, the lowest, or zeroth, order process (a) can be calculated in pure QED, while first order corrections, including real (b) and virtual (c) gluon radiation, also depend on the QCD coupling constant. These corrections have been calculated in [42] and were found to contribute 30% of the cross section in the direct case. It has also been shown that the direct part alone (including corrections) cannot reproduce the measurements of b and c quark production in e^+e^-, ep and pp collisions.

In the single resolved case (d-f), one of the photons splits up in a flux of quarks and gluons, where one of these gluons fuse with the other photon. The next-to-leading order corrections are shown in (e) and (f). Since this process depends on the quark and gluon distribution in the photon, it cannot be calculated using perturbative QCD, but must be treated phenomenologically. The direct and single resolved processes are predicted to give equal contributions to the cross section at $\sqrt{s} \approx 200$ GeV [42]. In (g) and (h) is shown the double resolved case, where both photons split up and create a heavy quark pair. This process gives a smaller contribution than the direct and single resolved processes, since it depends on $\alpha^2 \approx 0.014$, but it becomes increasingly important with increasing energy.

In e^+e^- reactions there are additional contributions to heavy quark production, which have been discussed in [43]. The most important contribution comes from initial or final state radiation of a γ^*/Z, which decays into a heavy quark pair. The cross section of other processes discussed in [43] are typically several orders of magnitude smaller at linear collider energies. Only the diagrams shown in Figure 2a, d, e and g have been taken into account in this analysis.

5 Higher order processes

The processes in Figure 2 are all of zeroth, first or second order in the strong coupling α_s, and the matrix elements have all been calculated using perturbative QCD. However, in high energy collisions it is possible to have many gluon emissions, making the zeroth, first and even second order calculations insufficient to decribe the data. Due to the self coupling of the gluons, the complexity of the processes increases rapidly with increasing order, making perturbative calculations very difficult. Instead one uses evolution equations to generate

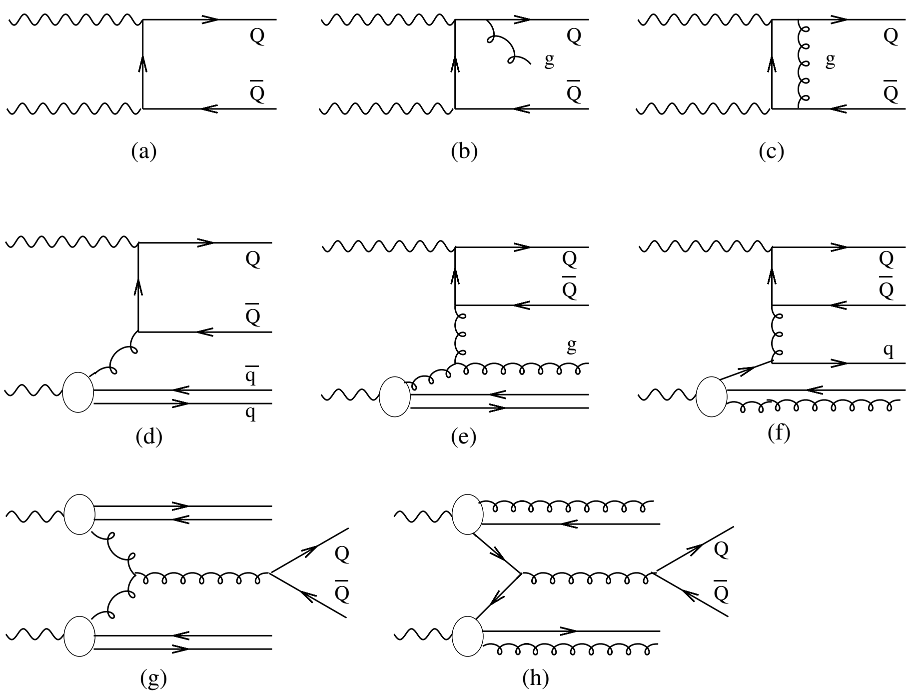

Figure 2: *Production mechanisms in heavy quark production.*

the higher order emissions. These equations describe, under certain approximations, how a mother parton is split into two daughter partons, one of which is emitted whereas the other continues as a propagator parton. The daughter propagator parton is then split into two daughters and so on. This creates a parton ladder, as illustrated in Figure 3. The general structure of an evolution equation is

$$f_j = f_0 + \int f_i \cdot P_{i \to j,k}$$

where f_i and f_j are the parton density functions for the mother and daughter propagator gluons, f_0 is the input gluon density function and $P_{i\to j,k}$ is the splitting kernel describing the probability that the parton i is split into two partons j and k. In the following discussion, the evolution starts at the bottom in Figure 3 and continues towards the quark box. The possible splittings are $q \to qg$, $g \to q\bar{q}$ and $g \to gg$. There are a number of different evolution equations, each one taking different parts of the full calculation into account and evolving the density functions in different variables. A short presentation of three different approaches follows, where the first is valid for large μ^2, the second is valid for small x and moderate μ^2, and the third is valid for both these regions. The latter is of special importance for this paper.

5.1 The DGLAP evolution

The DGLAP [44, 45, 46, 47] evolution equation is of the form

$$\frac{df_j(x,\mu^2)}{d\ln\mu^2} = \frac{\alpha_s(\mu^2)}{2\pi}\sum_i \int_x^1 \frac{dx'}{x'} f_i(x',\mu^2) P_{i\to j,k}(z) \tag{5}$$

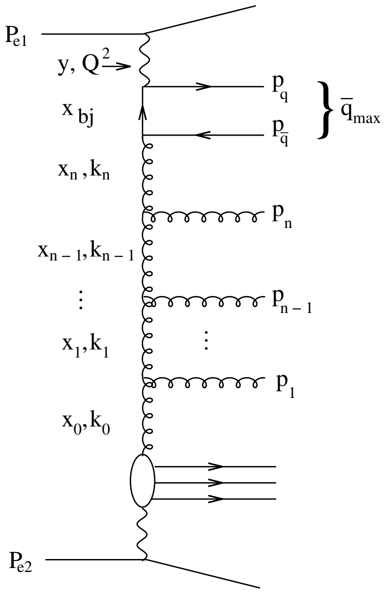

Figure 3: *Parton ladder created by gluon emissions.*

where $f(x, \mu^2)$ is the density of partons carrying a longitudinal momentum fraction x probed at a scale μ^2, and $P_{i \to j,k}(z)$ describes the probability that a parton i is split into two partons j and k with a fraction $z = \frac{x}{x'}$ and $1 - z$ of the original parton momentum, respectively. The probability that a gluon splits into two gluons is given by

$$P_{g \to g,g}(z) = \frac{1}{1-z} - 2 + z(1-z) + \frac{1}{z} \tag{6}$$

where the terms $\frac{1}{1-z}$ and $\frac{1}{z}$ are called the singular terms, since they give infinite contributions when $z \to 1$ and $z \to 0$, respectively. The equation (5) thus describes the probability change of finding a parton of type j with momentum fraction x as we increase the scale μ^2. In the DGLAP formalism, the gluon chain in Figure 3 is assumed to be strongly ordered in virtuality

$$\mu^2 \gg |k_n^2| \ldots \gg |k_1^2| \gg |k_0^2|, \tag{7}$$

where k_i is the four momentum of parton i. This means that in each splitting $i \to i+1, j$ one can approximate $k_0^2 = k_1^2 = \ldots\ k_i^2 = 0$ compared to k_{i+1}^2, and since $k_i^2 = m_i^2$ these partons are considered to be massless (or on-shell). It can be shown that the ordering in virtuality implies that also the transverse momentum of the propagator partons are strongly ordered (at small z) according to

$$\mu^2 \gg |k_{tn}^2| \ldots \gg |k_{t1}^2| \gg |k_{t0}^2| \tag{8}$$

where $k_{ti} = (0, k_{xi}, k_{yi}, 0)$. Hence, in each splitting one can approximate $k_{t0}^2 = k_{t1}^2 = \ldots\ k_{ti}^2 = 0$, which means that the DGLAP approach is a collinear approximation (which is obvious since there is no k_t-dependence in (5)). It can be shown, that using the DGLAP evolution is equivalent to resum terms of the form $(\alpha_s \ln(\mu^2))^n$ in the expansion of the cross section. Hence, the DGLAP approximation is only valid at large μ^2 where these terms will dominate.

5.2 The BFKL evolution

The BFKL [48, 49, 50] evolution equation resums the terms $(\alpha_s \ln(\frac{1}{x}))^n$ in the expansion, and is thus only valid at small x. It is of the form

$$\frac{d\mathcal{G}(x,k_t^2)}{d\ln(\frac{1}{x})} = \int dk_t^{'2} \mathcal{G}(x,k_t^{'2}) \cdot K(k_t^2,k_t^{'2}). \tag{9}$$

Here, the function K is the splitting kernel equivalent to P in (5). The evolution is made in increasing $\ln(\frac{1}{x})$, since

$$x_0^2 \gg x_1^2 \ldots \gg x_n^2 \gg x_{Bj}^2 \tag{10}$$

has been assumed. This implies that the emitted gluons will take a large fraction of the propagator momentum. However, there is no ordering in k^2 or k_t^2, so the collinear approximation can not be used, and the incoming partons of the matrix elements must be taken off-shell (the particles can have a virtual mass). Another important consequence of BFKL is that unintegrated parton densities must be used in (9), i.e. they must depend on k_t.

5.3 The CCFM evolution

The CCFM [29, 30, 31, 32] evolution equation is valid both at large and small x, since it resums terms of both the form $(\alpha_s \ln(\frac{1}{x}))^n$ and $(\alpha_s \ln(\frac{1}{1-x}))^n$. This means that at large x the CCFM evolution will be DGLAP-like, and at small x it will be BFKL-like. The CCFM evolution includes angular ordering in the initial state cascade, which means that the emission angles of the partons with respect to the propagator increases as one moves towards the quark box,

$$\Xi \gg \xi_n \gg \ldots \xi_1 \gg \xi_0, \tag{11}$$

where the maximum allowed angle Ξ is set by the hard quark box,

$$p_q + p_{\bar{q}} = \Upsilon(P_{e1} + \Xi P_{e2}) + \vec{Q}_t.$$

This is written in the Sudakov variables, where p_q, $p_{\bar{q}}$, P_{e1} and P_{e2} are the four momenta of the produced heavy quarks and the incoming particles, respectively (see Figure 3), Υ and $\Upsilon\Xi$ are the positive and negative light-cone momentum fractions of the heavy quark pair, and $\vec{Q}_t$ is the sum of the transverse momentum vectors of the heavy quark pair. The momenta of the emitted gluons can be written similary,

$$p_i = \upsilon_i(P_{e1} + \xi_i P_{e2}) + p_{ti}, \; \xi_i = \frac{p_{ti}^2}{s\upsilon_i^2}, \tag{12}$$

where $\upsilon_i = (x_{i-1} - x_i)$ is the momentum fraction of the emitted gluon, p_t is the transverse momentum of the gluon, and $s = (P_{e1} + P_{e2})^2$ is, as usual, the squared center of mass energy. Here, we have assumed that all particles are massless. The CCFM equation is written as

$$\bar{q}^2 \frac{d}{d\bar{q}^2} \frac{x\mathcal{A}(x,k_t^2,\bar{q}^2)}{\Delta_s(\bar{q}^2,\mu_0^2)} = \int dz \frac{d\phi}{2\pi} \frac{\tilde{P}(z,k_t^2,(\bar{q}/z)^2)}{\Delta_s(\bar{q}^2,\mu_0^2)} x'\mathcal{A}(x',k_t^{'2},(\bar{q}/z)^2)$$

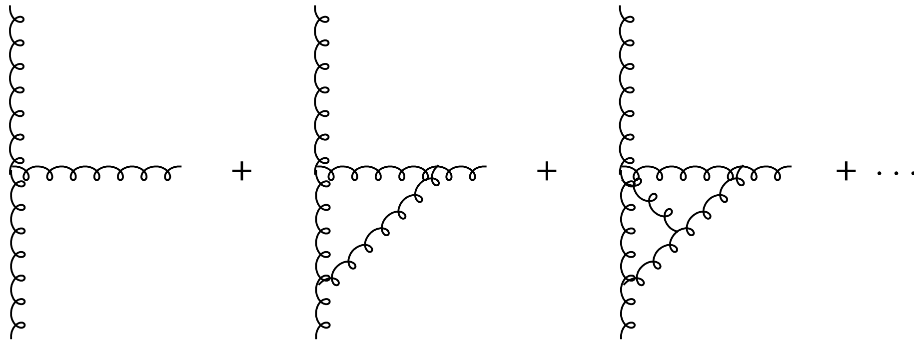

Figure 4: *The Reggeization of the gluon vertex.*

where

$$\bar{q}_i = \frac{p_{ti}}{1 - z_i} = x_{i-1}\sqrt{s\xi_i} \tag{13}$$

is the rescaled transverse momenta of the emitted gluons and $z_i = \frac{x_i}{x_{i-1}}$. In this formalism, (11) becomes

$$q_i > z_{i-1}q_{i-1}. \tag{14}$$

When $z \to 1$ we have $q_i > q_{i-1}$, i.e. ordering in rescaled transverse momentum, which means that the evolution is DGLAP-like. In the limit $z \to 0$ the angular ordering gives no restrictions on the rescaled transverse momentum. Also, (10) holds because of the definition of z. This means that the evolution is BFKL-like. The Sudakov form factor Δ_s describes the probability that there are no emissions from the starting scale μ_0^2 to the maximum rescaled transverse momentum $\bar{q}^2_{max}$. The CCFM splitting function $\tilde{P}$ is defined as

$$\tilde{P}_g(z, k_t^2, (\bar{q}/z)^2) = \frac{\bar{\alpha}_s(q_i^2(1-z_i)^2)}{1 - z_i} + \frac{\bar{\alpha}_s(k_{ti}^2)}{z_i}\Delta_{ns}(z_i, k_{ti}^2, q_i^2), \tag{15}$$

which is somewhat different than the DGLAP splitting function (6). First of all, the CCFM splitting function only includes the singular parts of the DGLAP splitting function. The other difference is that there is one additional function Δ_{ns}, called the non-Sudakov form factor, in (15). The non-Sudakov form factor originates from the fact that, in CCFM and BFKL, all virtual corrections in the gluon vertex are automatically taken into account, see Figure 4. This is called the Reggeization of the gluon vertex.

6 Monte Carlo simulations

As was already mentioned, higher order processes are very difficult to calculate using perturbative QCD. Moreover, it is not quarks that are detected in the experiments, but hadrons. The transition from parton level (Figure 2, for example) to hadron level takes place over long distances where α_s is large. Hence, perturbation theory is not valid here. To overcome this problem, Monte Carlo (MC) generators are used. For each event, these programs generate all the particles, their four-momenta and all the kinematic variables according to certain theoretical prescriptions. The higher order gluon emissions are simulated by evolving the parton ladder according to some evolution equation (DGLAP, BFKL, CCFM etc.), and the transitions to hadron level can also be implemented via hadronization models.

6.1 CASCADE

The Monte Carlo generator CASCADE [51] is based on the CCFM evolution equation and thus uses unintegrated parton desities and off-shell matrix elements. For technical reasons, a backward evolution is used, where first the hard scattering is generated and then the initial state cascade (the gluon ladder) is evolved from the quark box to the incoming particles. In this evolution only gluon emissions are treated, that is, only the splitting $g \to gg$ is considered. CASCADE also performs the hadronization, using the Lund string model in JETSET/PYTHIA [52].

7 The unintegrated gluon density

The evolution machinery was first tested using the one-loop (DGLAP-like) evolution for the proton and the photon. Then, the unintegrated gluon density for the photon was obtained using the full CCFM evolution. The uncertainties in the evolution are discussed in section 7.5. Since the distributions obtained with the CCFM evolution were compared with the derivative of standard gluon density functions, taken from [53], a short discussion of the differentiation method will be given first. Alternative methods to calculate the unintegrated gluon density can be found in [28, 54].

7.1 Numerical differentiation method

Two numerical differentiation methods were tested: DDERIV [55] and DFRIDR [56], which are based on Rombergs principle of sequence extrapolation and Richardson's deferred approach to the limit, respectively. The first test was to differentiate the simple function $f(x) = -\frac{1}{x}$ with respect to x. Here, both methods gave good results, but only after adjusting a parameter in DDERIV. A second test was to differentiate the GRV[1] [57] density function with respect to the scale μ^2, then to integrate over k_t^2 and compare the results with the original GRV distribution. This was done because we will later use equation (4) which relates the unintegrated parton density function $\mathcal{G}(x, k_t^2)$ to the integrated one $g(x, \mu^2)$. The adaptive Gaussian method taken from [58] was used for the integration. As seen in Figure 5, the DFRIDR routine reproduced the distribution succesfully, except in the high x region which will be discussed later. However, with the same value of the parameter as used above, the DDERIV approach gave unacceptable results, and only after changing this parameter again the obtained distribution (which is shown in the figure) started to resemble the original one. Because of this poor reproduction of the input distribution, and its sensitivity to the choice of parameter, we decided to use DFRIDR instead of DDERIV.

[1] GRV-G HO (GRV for the photon) was used.

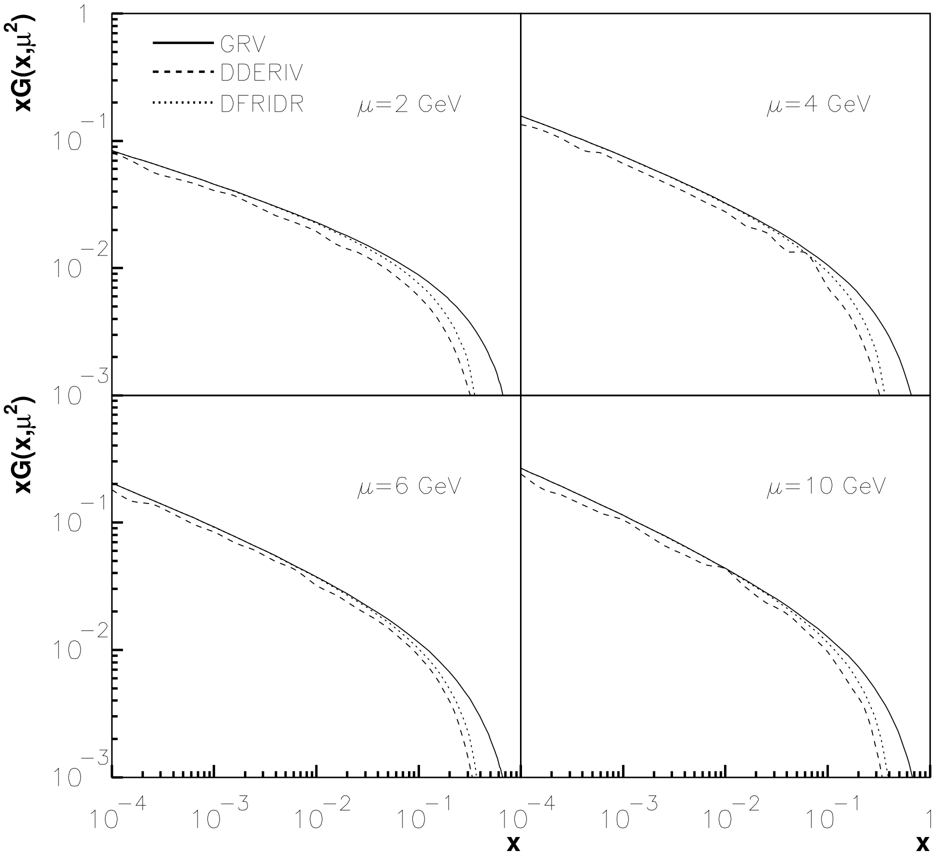

Figure 5: *The GRV distribution differentiated with DFRIDR and DDERIV, and then integrated, compared with the original GRV distribution.*

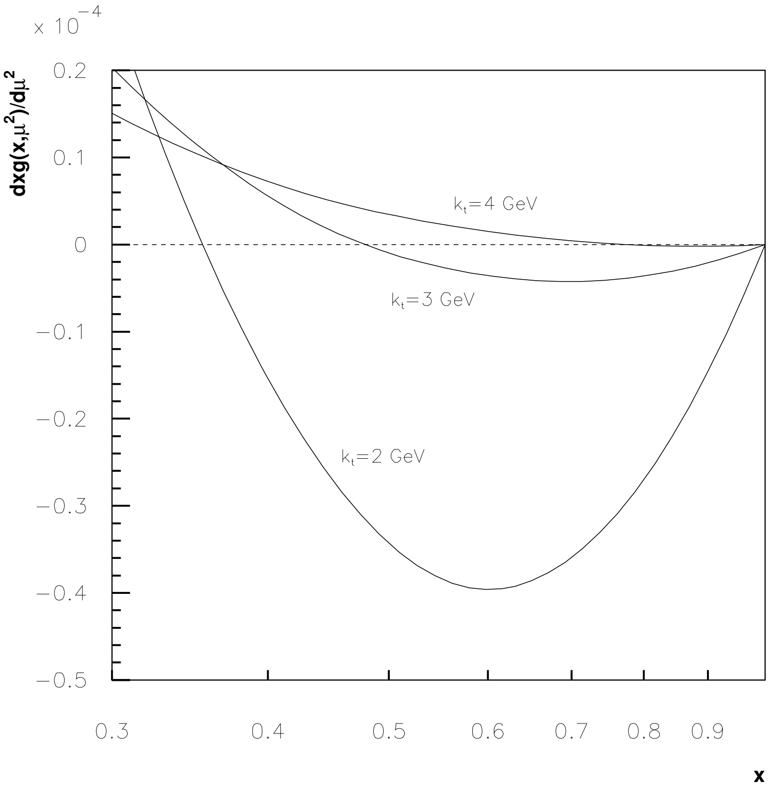

Figure 6: $\mathcal{G}(x, k_t^2)$ *as a function of* x *for different values of* $\mu = k_t$*. When the function becomes negative, the differentiation method of obtaining the unintegrated gluon density becomes invalid.*

The deviations from the original distribution at high x is due to the fact that the function (4) becomes negative in this region. This is because of the scaling violation: as the scale μ^2 increases, smaller distances are resolved and as a consequence we resolve more gluons with small x (i.e. $x < 0.1$) and less gluons with high x. In Figure 6 is shown how the point, where the derivative becomes negative, changes with $\mu = k_t$. The smallest x-value for this point is obtained with $k_t = 2$ GeV, where $x \approx 0.35$. Since $\mathcal{G}(x, k_t^2)$ is interpreted as a probability, the method becomes invalid at such high x.

7.2 Evolution of the unintegrated gluon density

The evolution of the unintegrated gluon density was made using the CCFM equation in a forward evolution procedure based on the Monte Carlo technique as described in [59]. An initial gluon distribution is chosen as well as a starting scale μ_s and a rescaled transverse momentum $\bar{q}_s$, which is related to the emission angle (see equations (12) and (13)), for the first emitted gluon. The default values $\mu_s = \bar{q}_s = 1.4$ GeV was obtained by a fit to the proton structure function [59]. The evolution then starts with $\bar{q}_{max,0} = \bar{q}_s$, and k_{t0} chosen from a Gaussian distribution around μ_s to simulate a Fermi motion of the partons. x_0 is chosen from the initial gluon distribution using the Monte Carlo method. The branching is then repeated until the next emitted gluon would have a higher $\bar{q}$ than

$\bar{q}_{max,0}$. This is repeated 10^7 times for each of the 50 different maximum $\bar{q}_{max,i}$ chosen from $\bar{q}_{max,0} = \bar{q}_s < \bar{q}_{max,i} < \bar{q}_{max,50} = 1800$ GeV in steps of $log(\bar{q}_{max})$, thus giving a distribution $\mathcal{A}(x, k_t^2, \bar{q}^2)$ in a $50 \times 50 \times 50$ grid of $log(x)$, $log(k_t^2)$ and $log(\bar{q}_{max})$. For values between the gridpoints the method of linear interpolation is used. With the unintegrated parton distribution avaliable, a backward evolution scheme can be used for the simulation of the parton emissions.

7.3 One-loop evolution

To make sure that the evolution procedure is working, the evolution was first made for the proton with a GRV[2] input distribution (using the default values $\mu_s = \bar{q}_s = 1.4$ GeV) and using the one-loop approximation [60, 61, 62], which means that the CCFM evolution is reduced to the DGLAP evolution, with the difference that the CCFM one-loop evolution still treats the full kinematics, i.e. it takes the transverse momentum k_t into account. This is done by putting $\Delta_{ns} = 1$ in the splitting function (15) and reducing the condition (14) to ordering in transverse momentum (8). The obtained distribution $x\mathcal{A}(x, k_t^2, \bar{q}^2)$ was then integrated over k_t^2,

$$\int_0^{\bar{q}^2} dk_t^2 x\mathcal{A}(x, k_t^2, \bar{q}^2) = x\mathcal{G}(x, \bar{q}^2), \tag{16}$$

and compared to the original GRV distribution at different scales, see Figure 7. The small differences are due to the fact that the splitting function only contains the singular parts, and that only the splitting $g \rightarrow gg$ is considered. Nevertheless, the distributions are still in good agreement which indicates that the evolution machinery is working.

The situation for the photon is a bit different, since the structure function, in addition to the hadronic component, now also consists of a pointlike component which reflects the splitting of the photon into a quark-antiquark pair. Also, there are no sum rules equivalent to those in the proton case that constrain the quark distributions in the photon. However, these differences do not matter, since we only use the gluon distribution and the gluon splitting $g \rightarrow gg$. Figure 8 shows the evolved distribution for the photon, using the same parameters as in the proton case and the GRV[3] as input distribution, compared to the input distribution at different scales. The one-loop evolved and the GRV distributions show a similar behaviour, although the one-loop evolved distribution is a bit steeper at large scales. It is not surprising that the one-loop evolution does not give equally good agreement in the proton and the photon case, since the same parameters have been used in both one-loop evolutions, while different techniques and starting scales for the proton and the photon were used to obtain the original GRV distributions.

From the above we conclude that the one-loop evolution is able to reproduce the input distributions reasonably well, and hence that the evolution machinery is working for the CCFM one-loop case. A similar test cannot be done for the full CCFM evolution, since the obtained distributions should be different from the ones obtained with CCFM one-loop evolution. However, it has already been shown [59] that the CCFM evolution is working for the proton, in the sense that it can explain data, for example $b\bar{b}$ production at the

[2] GRV 98 LO was used
[3] GRV-G LO was used

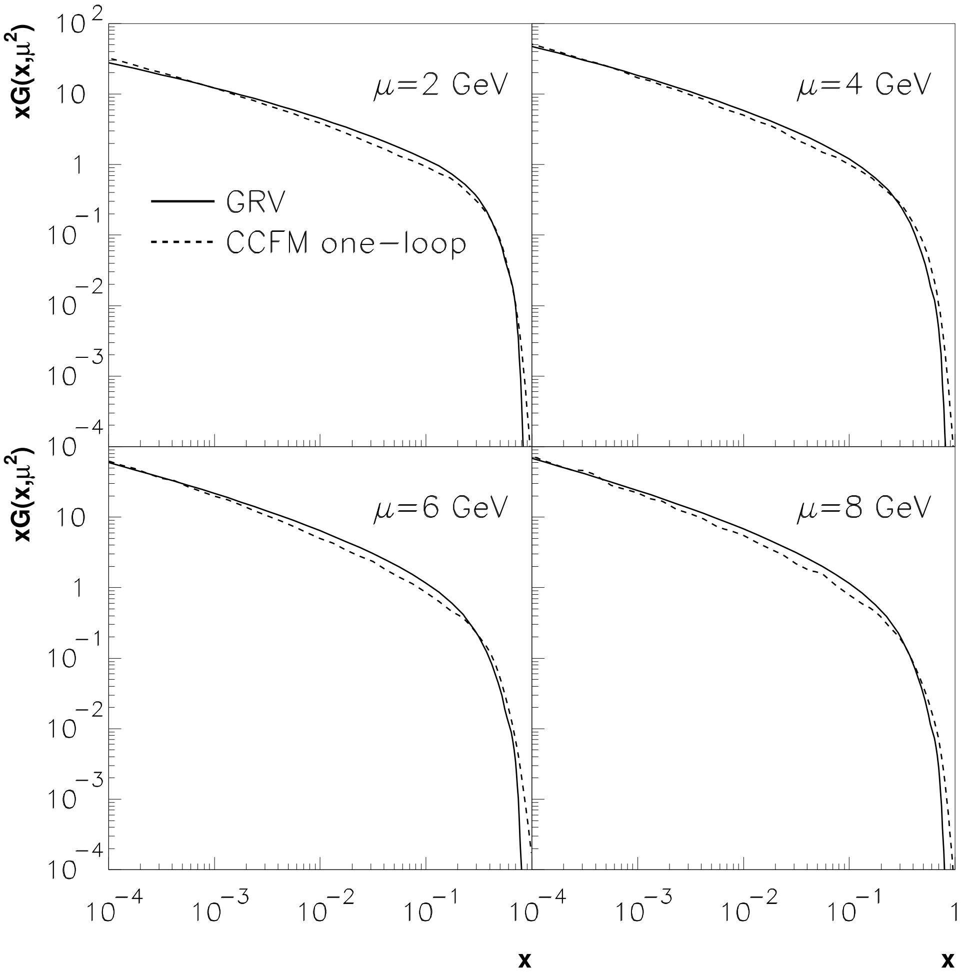

Figure 7: *The integrated CCFM one-loop evolved distribution for the proton compared to the GRV distribution at different scales.*

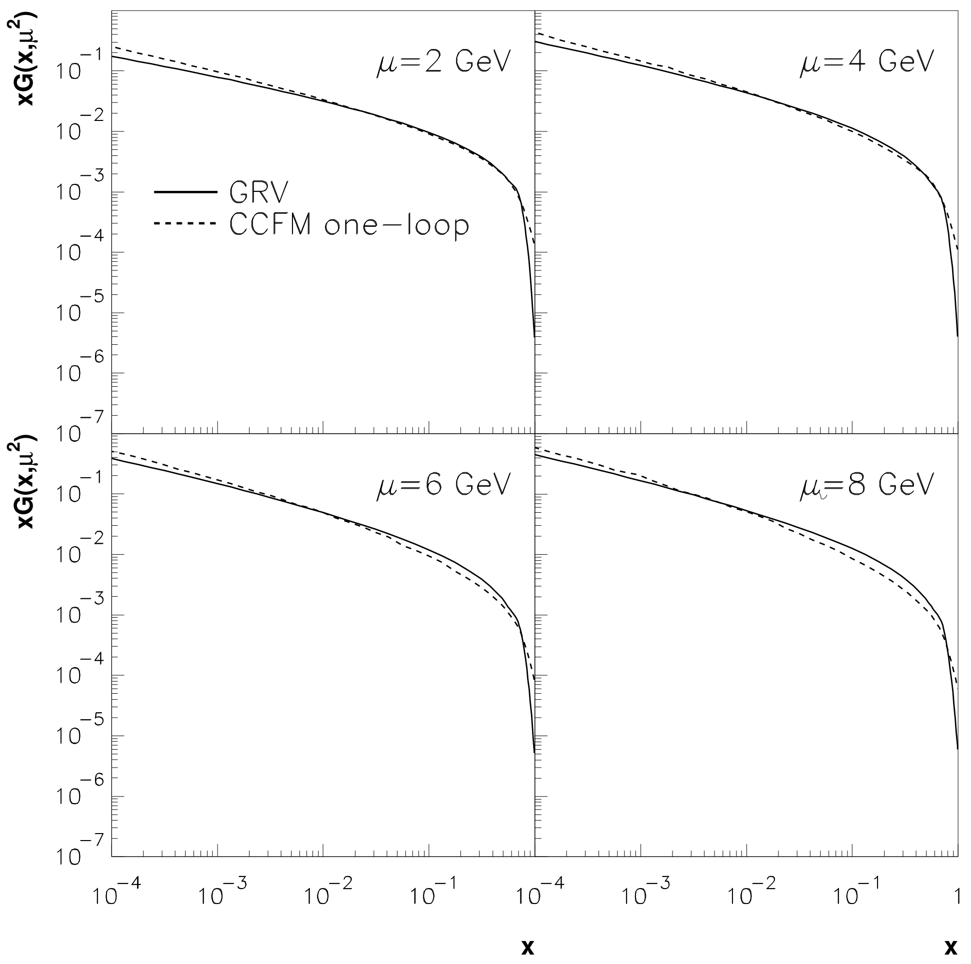

Figure 8: *The integrated CCFM one-loop evolved distribution for the photon compared to the GRV distribution at different scales.*

TEVATRON, which could not be explained with other methods. Since the only difference between the photon and proton evolution is the starting distribution, it can be assumed that the CCFM evolution will work also for the photon.

7.4 CCFM evolution

After making sure that the parton evolution scheme gives consistent results, the unintegrated gluon density for the photon was evolved using the full CCFM evolution procedure. The obtained distributions integrated over k_t^2 are compared in Figure 9 to the GRV[4] distribution, which was used as input distribution. One of the more obvious differences is that the CCFM evolved distribution is much higher than the original GRV. This is due to differences in the definition of the integrated gluon density; one can either integrate over d^2k_t or over dk_t^2. The difference is a factor π, which explains the main part of the normalization difference. We can also note that the CCFM evolved distribution is less steep than the original GRV. This is a consequence of that the non-Sudakov form factor $\Delta_{ns} \to 0$ when $z \to 0$ and thereby screens the $\frac{1}{z}$ factor in the splitting function. This results in a lower splitting probability compared to the DGLAP case (where $\Delta_{ns} = 1$) which becomes visible in the small x (small z) region where the factor $\frac{1}{z}$ dominates the splitting function.

In Figure 10 is shown the unintegrated distribution as a function of x for different values of k_t, and as a function of k_t^2 for different values of x, compared to the derivative of GRV. Here, $\mu = \bar{q} = 10$ GeV. Also in Figure 10a we see that the CCFM distribution in general is higher (except at very high k_t) and we can also see the non-Sudakov supression at small x. We should also remember that the derivative method becomes invalid at high x because $\frac{dg(x,\mu^2)}{d\mu^2}$ becomes negative. This explains the big difference between the CCFM evolved distribution and the GRV at $k_t = 2$ GeV, because the derivative becomes negative already at $x \approx 0.35$ (see Figure 6). In Figure 10b one can see the typical exponential k_t-dependence of the derivative of GRV. Since the GRV distribution is only defined for $\mu^2 = k_t^2 \geq 0.3$ GeV^2, it is replaced with $\frac{x\mathcal{G}(x,k_{t0}^2)}{k_{t0}^2}$ for $k_t^2 < k_{t0}^2 = 0.3$ GeV^2 [63]. We can also note that the probability for the gluons to have a $k_t^2 > \mu^2 = 100$ GeV^2 in the CCFM approach is significant, which would not be possible using DGLAP. This is a consequence of the k_t^2-ordering in the DGLAP evolution, where k_t^2 is always less than μ^2, see (8), and the non-ordering in k_t^2 in the CCFM evolution, where the gluons can have any kinematically allowed value of k_t^2.

7.5 Uncertainties

In the evolution of the unintegrated gluon distributions above, the GRV density was used as input distribution, with $\mu_s = \bar{q}_s = 1.4$ GeV given from a fit to the parton density of the proton [59]. A natural question is how sensitive the results are to the selected starting distribution and the parameters chosen. Therefore, the evolution was made also with the SaS[5] [64] parton distribution as input (and keeping $\mu_s = \bar{q}_s = 1.4$ GeV), and also with the GRV parametrization as input but with $\mu_s = 1.4$ GeV and $\bar{q}_s = 1.2$ GeV, $\mu_s = 1.4$ GeV

[4]GRV-G HO was used

[5]SaS-G 1D was used

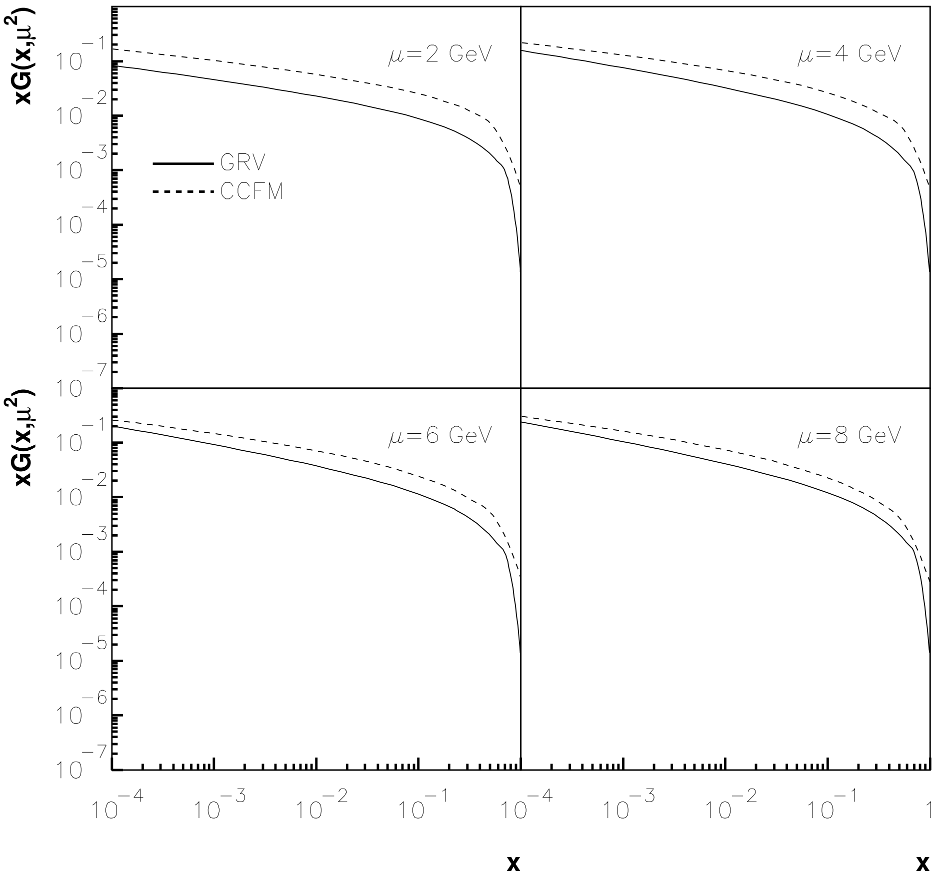

Figure 9: *The integrated CCFM evolved distribution for the photon compared to the GRV distribution at different scales.*

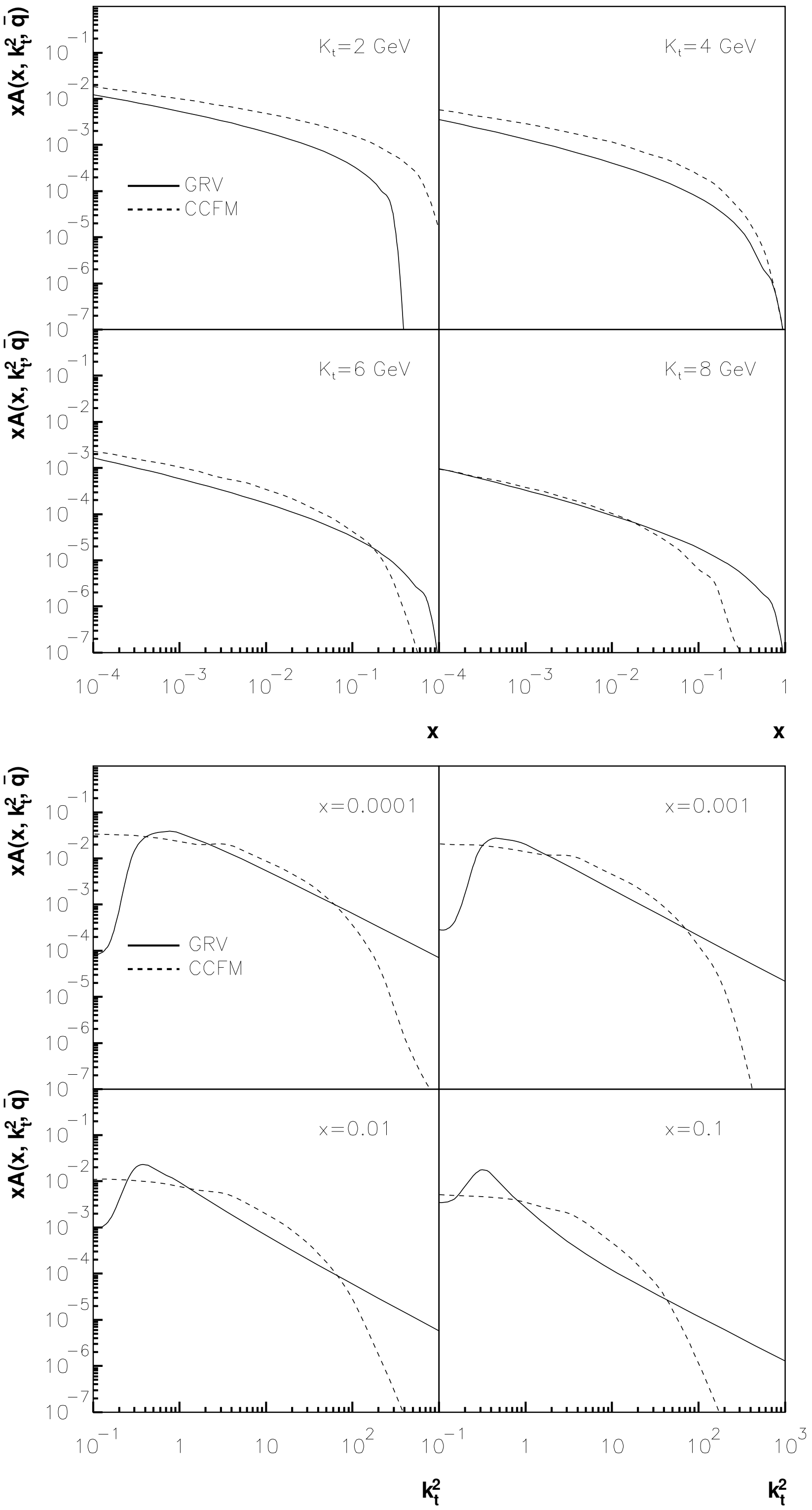

Figure 10: *The unintegrated CCFM evolved distribution for the photon compared to the derivative of the GRV distribution as a function of x for different values of k_t (a), and as a function of k_t^2 for different values of x (b).*

and $\bar{q}_s = 1.6$ GeV, and $\mu_s = 1$ GeV and $\bar{q}_s = 1.4$ GeV. The various distributions obtained are compared to the previous ones in Figure 11 and 12. When comparing the integrated distributions (Figure 11) we see that there is only a weak dependence on the starting value $\bar{q}_s$, such that the distribution becomes somewhat flatter at large $\bar{q}_s$. This can be understood, since a larger starting angle would mean that it takes less emissions to reach the maximum value (since there is angular ordering), and less emissions would mean that the gluon entering the matrix element (gluon n in Figure 3) would have a larger longitudinal momentum fraction x. A change in μ_s makes a significant difference, where a smaller μ_s gives a distribution which is lower at small x. One can also see that the evolution depends on the choice of input distribution, where the main features of the input distribution remains after the evolution, see also Figure 13.

Also when comparing the unintegrated gluon densities in Figure 12, we see that the dependence on $\bar{q}_s$ is small while changing μ_s makes a significant difference, especially in the region $1 < k_t^2 < 10$. This is probably due to details in the evolution: In order to avoid soft emissions a cut-off scale μ_s is defined. Thus if the propagator gluon has $k_t > \mu_s$ a real emission is allowed, but it is not if $k_t < \mu_s$. Since there is no ordering in k_t in the CCFM evolution any propagator gluon along the evolution chain might get $k_t < \mu_s$ after a real emission. In that case, the evolution of the propagator is continued until $k_t > \mu_s$ and a real emission is allowed.

8 Heavy quark cross sections

The obtained unintegrated gluon density was used as an input to the MC generator CASCADE to calculate heavy quark cross sections in e^+e^- collisions, which are compared to LEP data. Also, predictions for heavy quark cross sections in e^+e^- and $\gamma\gamma$ collisions at TESLA energies are given.

8.1 Cross section calculation test

The e^+e^- cross sections can be calculated using the relation

$$\sigma_{e^+e^-\to e^+e^- b\bar{b},c\bar{c}X} = \int \frac{dQ_1^2}{Q_1^2}\frac{dQ_2^2}{Q_2^2}\mathcal{L}_{\gamma\gamma}(W_{\gamma\gamma},Q_1^2,Q_2^2)\sigma_{\gamma\gamma\to b\bar{b},c\bar{c}X}(W_{\gamma\gamma})dW_{\gamma\gamma} \tag{17}$$

where $\mathcal{L}_{\gamma\gamma}$ is the photon flux in the electron, $W_{\gamma\gamma}$ is the center of mass energy in the $\gamma\gamma$ system, Q_i is the virtuality of photon i and $\sigma_{\gamma\gamma\to b\bar{b},c\bar{c}X}$ is the cross section for the subprocess $\gamma\gamma \to b\bar{b}, c\bar{c}X$.

The direct and single resolved cross sections for b and c quark production in e^+e^- collisions were calculated with CASCADE and compared with the results in [42]. Since the direct cross section is independent of the gluon content in the photon, and hence independent of evolution equations, these cross sections should agree. In heavy flavour production, CASCADE uses off-shell matrix elements as calculated in [37]. Errors were found in [37] (eq. B16) where a factor $N_c e_q^2$ was missing in the direct cross section ($N_c = 3$ being the color factor and e_q being the EM charge of the produced quarks). With these

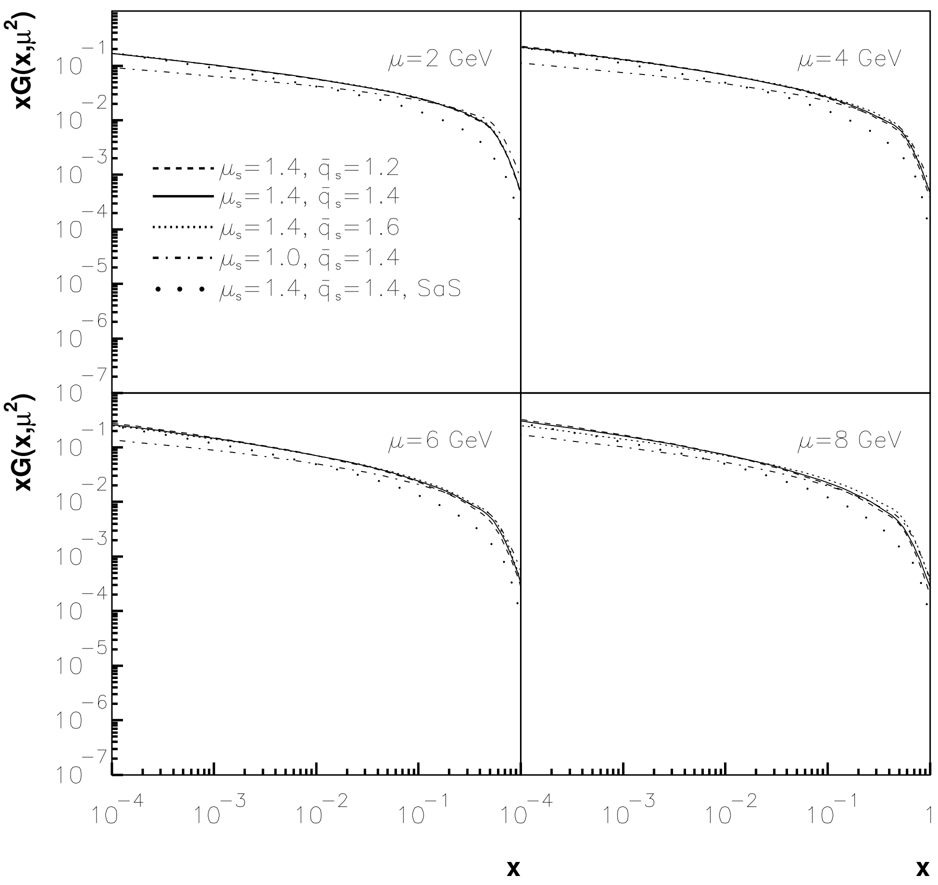

Figure 11: *The integrated CCFM evolved distributions for the photon with different combinations of μ_s, $\bar{q}_s$ and input distributions.*

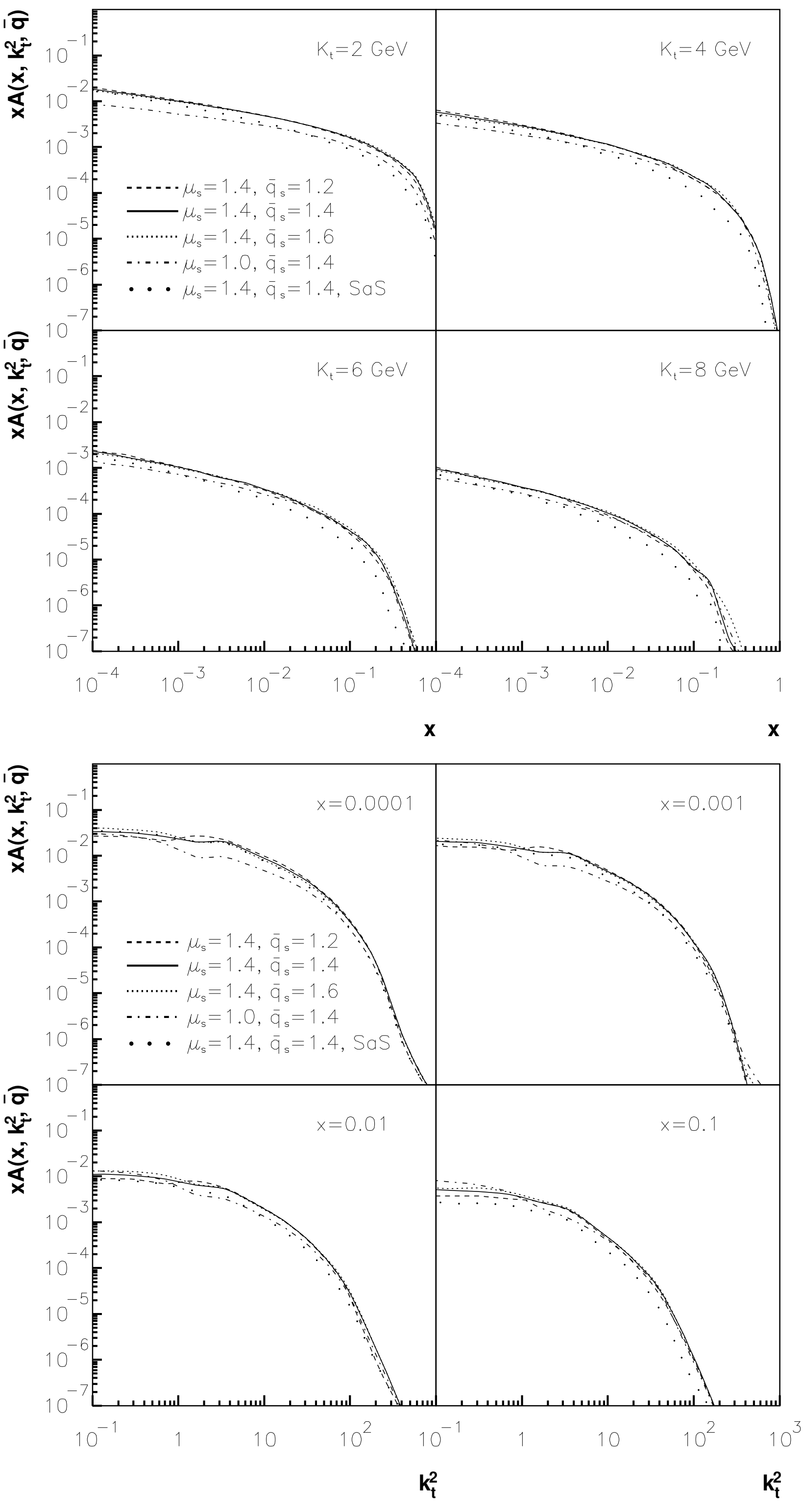

Figure 12: *The unintegrated CCFM evolved distributions for the photon with different combinations of μ_s, $\bar{q}_s$ and input distributions.*

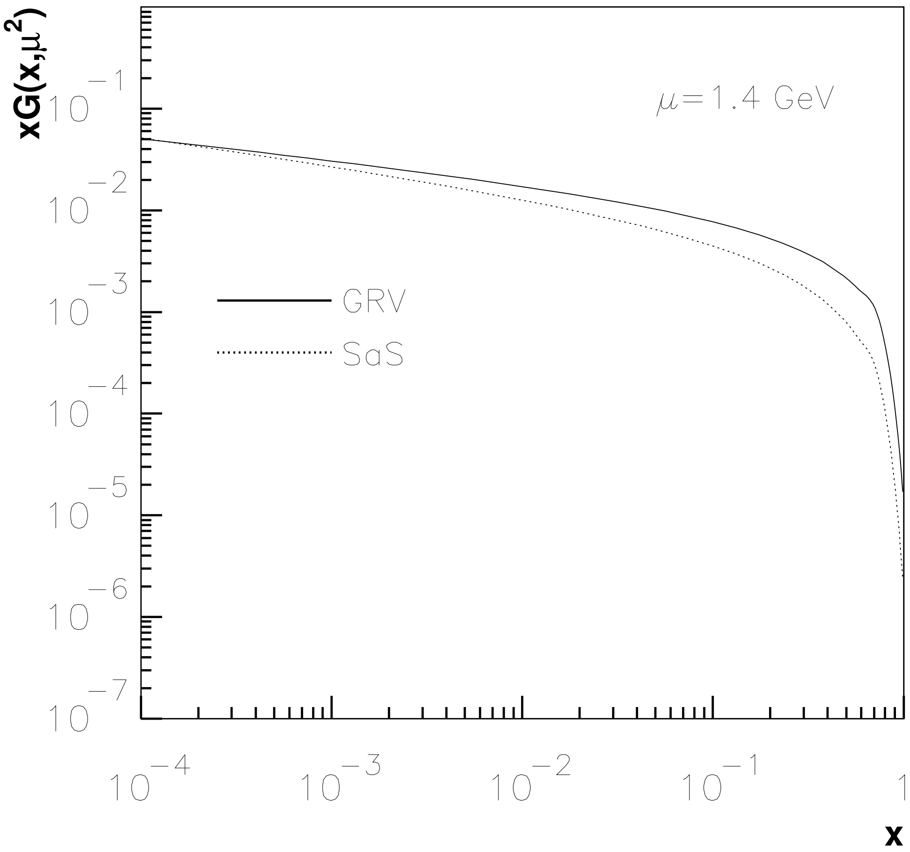

Figure 13: *The GRV and SaS distributions compared at the starting scale $\mu = 1.4$ GeV.*

factors taken into account, the direct cross sections from CASCADE and from leading and next-to-leading order calculations [42] were in good agreement, see Table 1. For the single resolved case, the DGLAP evolution was used with the gluon density according to GRV[6] to describe the photon structure and with cuts and parameters as in [42]. As seen, also these cross sections where in good agreement. The aim of this comparison is just to show that the basic machinery for cross section calculations in CASCADE is working.

CHARM

$\sqrt{s}$	$\sigma_{DIR}(pb)$		$\sigma_{1-RES}(pb)$	
(GeV)	*DREES*	*CASCADE*	*DREES*	*CASCADE*
180	296.8 (396.3)	328	269.9 (305.8)	217
91.2	191.2 (254.8)	213	93.38 (109.5)	80

BEAUTY

$\sqrt{s}$	$\sigma_{DIR}(pb)$		$\sigma_{1-RES}(pb)$	
(GeV)	*DREES*	*CASCADE*	*DREES*	*CASCADE*
180	1.280 (1.582)	1.35	1.371 (1.644)	1.19
91.2	0.663 (0.823)	0.71	0.302 (0.371)	0.27

Table 1: *Direct and single resolved charm and beauty cross sections calculated with CASCADE and compared to leading and next-to-leading order (in parenthesis) calculations in [42] (DREES). Here, $\mu^2 = 2m^2$, $\Lambda = 0.34$ GeV, $m_b = 4.75$ GeV and $m_c = 1.6$ GeV. In CASCADE, the scale factor 0.5 was used to obtain the correct scale.*

8.2 e^+e^- cross sections at LEP

In Figure 14 are shown the obtained cross sections for b and c quark production in e^+e^- collisions calculated with the k_t-factorization approach, using off-shell ME and a CCFM unintegrated gluon density evolved from a starting distribution given by GRV, compared to the collinear (DGLAP) predictions and data [1, 2, 7, 8, 9, 10]. Here, the masses $m_b = 4.5, 4.75, 5$ GeV and $m_c = 1.3, 1.5, 1.7$ GeV were used for the CCFM cross sections, while $m_b = 4.75$ GeV and $m_c = 1.5$ GeV were used for the cross sections calculated with DGLAP. This variation of the quark masses gives an estimate of the uncertainty in the calculation. One can see that the k_t-factorization approach describes the charm data reasonably well and that it gives larger cross sections compared to the collinear method. One can also see that the choice of mass makes a significant difference, such that a smaller mass gives a larger cross section. Nevertheless, the cross sections obtained with 1.3 GeV$< m_c <$ 1.7 GeV all lie within the experimental uncertainties.

The cross sections for $b\bar{b}$ production, on the other hand, are not well described. However, in the CCFM approach, one has to determine carefully the normalization of the cross sections. The reason for this is that the normalization of the unintegrated gluon density does not have to be the same as for the standard gluon densities generated according to the collinear scheme, since the integration is made over different regions (i.e. the integral

[6] GRV-G 1HO was used, as in [42]

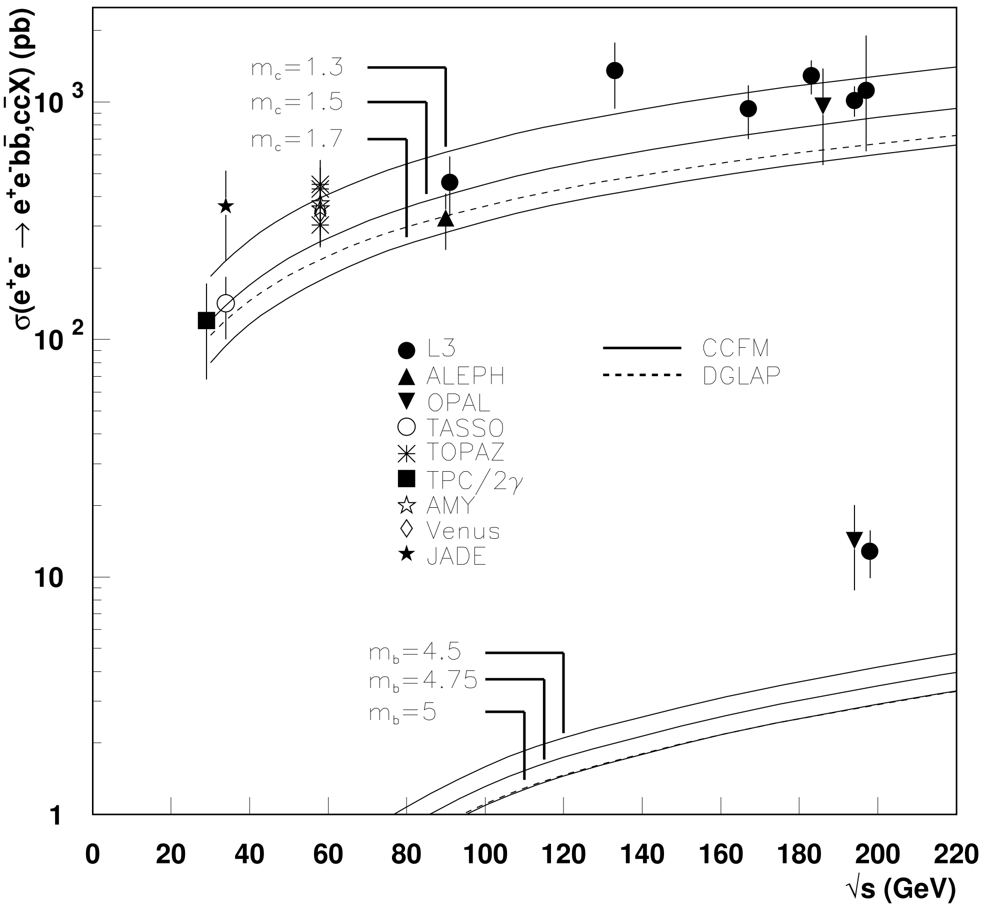

Figure 14: *The charm and beauty cross sections calculated with k_t-factorization compared to the DGLAP approach and data.*

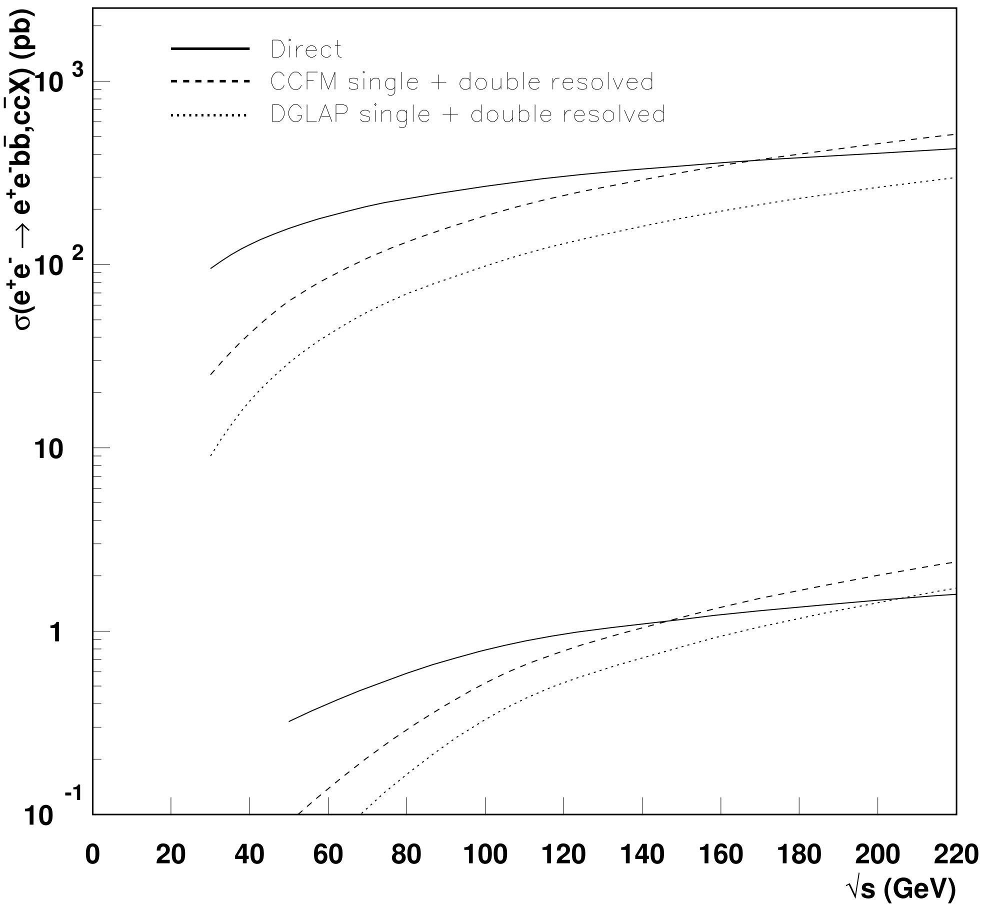

Figure 15: *The direct and resolved cross sections in heavy quark production calculated with CCFM and DGLAP.*

over dk_t^2 is from 0 to μ^2 in the collinear approach, whereas in the CCFM formalism the integral is over all kinematically allowed k_t^2) and the matrix elements are different. This normalization factor has to be applied to the single and double resolved cross sections, but not to the direct cross section since it is independent of the gluon density. The contribution of the direct and resolved cross sections are shown in Figure 15. As seen, the differences between CCFM and DGLAP are due to differences in the resolved contributions of the cross sections. Normalizing the CCFM cross section to the charm data at $\sqrt{s} = 200$ GeV for $m_c = 1.5$ GeV, by applying a normalization factor $n = 1.7$ to the single and double resolved cross sections, gives a much steeper behaviour of the total cross section, as seen in Figure 16. However, the CCFM predictions are still in good agreement with the charm data at $\sqrt{s} < 200$ GeV. The normalization also improves the situation for the $b\bar{b}$ cross section, where our calculations give $\sigma_{b\bar{b}} = 4.9$ pb at $\sqrt{s} = 200$ GeV. This can be compared to standard collinear NLO predictions which give $\sigma_{b\bar{b}} \approx 4$ pb [7] and results based on [28], giving $\sigma_{b\bar{b}} = 1.9$ pb using a KMR gluon density, and $\sigma_{b\bar{b}} = 2.7$ pb using a GBW gluon density at the same energy. The CCFM cross sections are of the same order but a bit larger than NLO standard calculations, which has also been observed in *ep* collisions at HERA. Thus, the improvement is not sufficient fully to describe the $b\bar{b}$ data, which is still

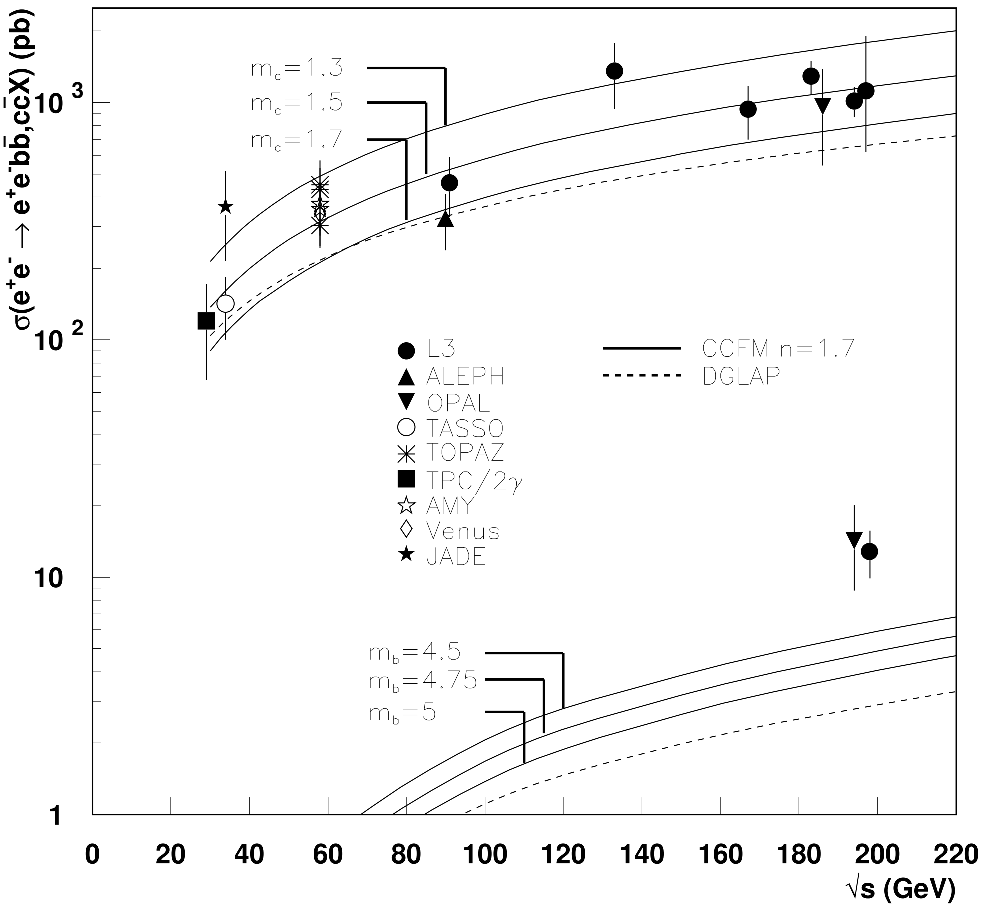

Figure 16: *The cross sections for heavy quark production calculated with CCFM and normalized to charm data at* $\sqrt{s} = 200$ *GeV with a factor* $n = 1.7$*, compared to DGLAP predictions and data.*

a factor 2-3 above predictions.

8.3 e^+e^- and $\gamma\gamma$ cross sections at TESLA

The CCFM predictions for heavy quark production in e^+e^- collisions at TESLA energies are shown in Figure 17. Here, the normalization factor $n = 1.7$ has been applied for the resolved cross sections. With a charm mass of $m_c = 1.5$ GeV the CCFM predictions at $\sqrt{s} = 500$ (800) GeV are

$$\sigma_{e^+e^-\to e^+e^- c\bar{c}X} = 2770\ (4165)\ \text{pb}.$$

For beauty, the predictions are

$$\sigma_{e^+e^-\to e^+e^- b\bar{b}X} = 17.06\ (30.72)\ \text{pb}$$

using a beauty mass of $m_b = 4.75$ GeV.

Figure 18 shows the charm and beauty cross sections in $\gamma\gamma$ collisions at TESLA energies calculated using the CCFM evolution. The normalization factor $n = 1.7$ has been applied to the resolved contributions. At $\sqrt{s} = 500$ (800) GeV, the predicted cross sections are

$$\sigma_{\gamma\gamma\to c\bar{c}X} = 269\ (359)\ \text{nb}$$

for charm and

$$\sigma_{\gamma\gamma\to b\bar{b}X} = 4.18\ (6.38)\ \text{nb}$$

for beauty. Also here, the masses $m_c = 1.5$ GeV and $m_b = 4.75$ GeV were used. Figure 18 also shows the resolved contributions of the cross sections. As seen, the single and double resolved cross sections dominate the total cross section at these energies. The reason for this is that the direct contribution, in contrast to the resolved ones, decreases with energy, and is only about 1% of the total cross section at $\sqrt{s} = 100$ GeV.

8.4 Uncertainties

The cross section for heavy quark production depends on the unintegrated gluon density and the partonic cross section. These in turn depend on a few parameters which are not fixed by theory but have to be determined from fits to experimental data, and therefore give rise to some uncertainties in the calculations. These uncertainties are discussed below and shown in Figure 19 for e^+e^- collisions.

The CCFM evolution of the unintegrated gluon density is sensitive to the input gluon density, the starting scale μ_s and the starting value for the rescaled transverse momentum $\bar{q}_s$. The default values in this analysis are $\mu_s = \bar{q}_s = 1.4$ GeV, obtained from a fit to the parton distribution in the proton [59], with a GRV input distribution. The gluon densities obtained with $\mu_s = 1$ GeV and $\bar{q}_s = 1.4$ GeV, and SaS input distribution with $\mu_s = \bar{q}_s = 1.4$ GeV showed the largest differences compared to the gluon density obtained

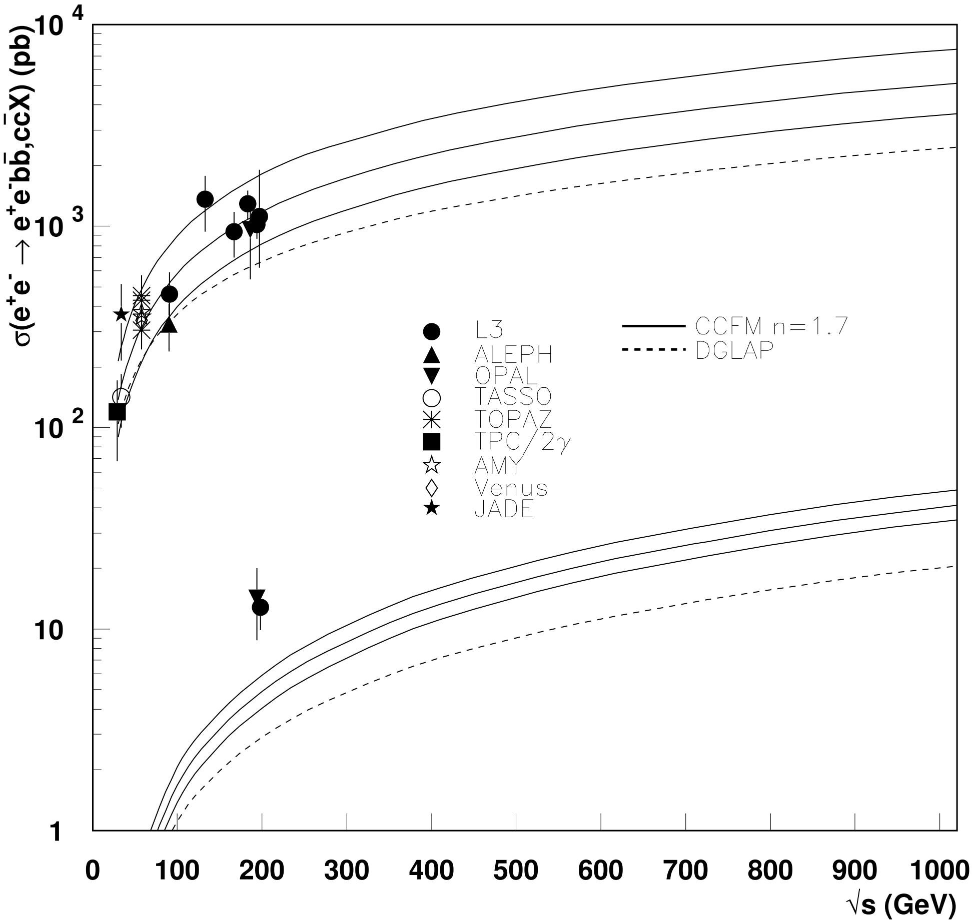

Figure 17: *Heavy quark cross section predictions for e^+e^- collisions at TESLA energies calculated with CCFM and compared to the DGLAP predictions. For CCFM, the quark masses $m_c = 1.3, 1.5, 1.7$ GeV and $m_b = 4.5, 4.75, 5$ GeV were used, where the smallest mass gives the largest cross section. For DGLAP, $m_c = 1.5$ GeV and $m_b = 4.75$ GeV. Also, the normalization factor $n = 1.7$ was applied to the resolved cross sections in the CCFM calculations.*

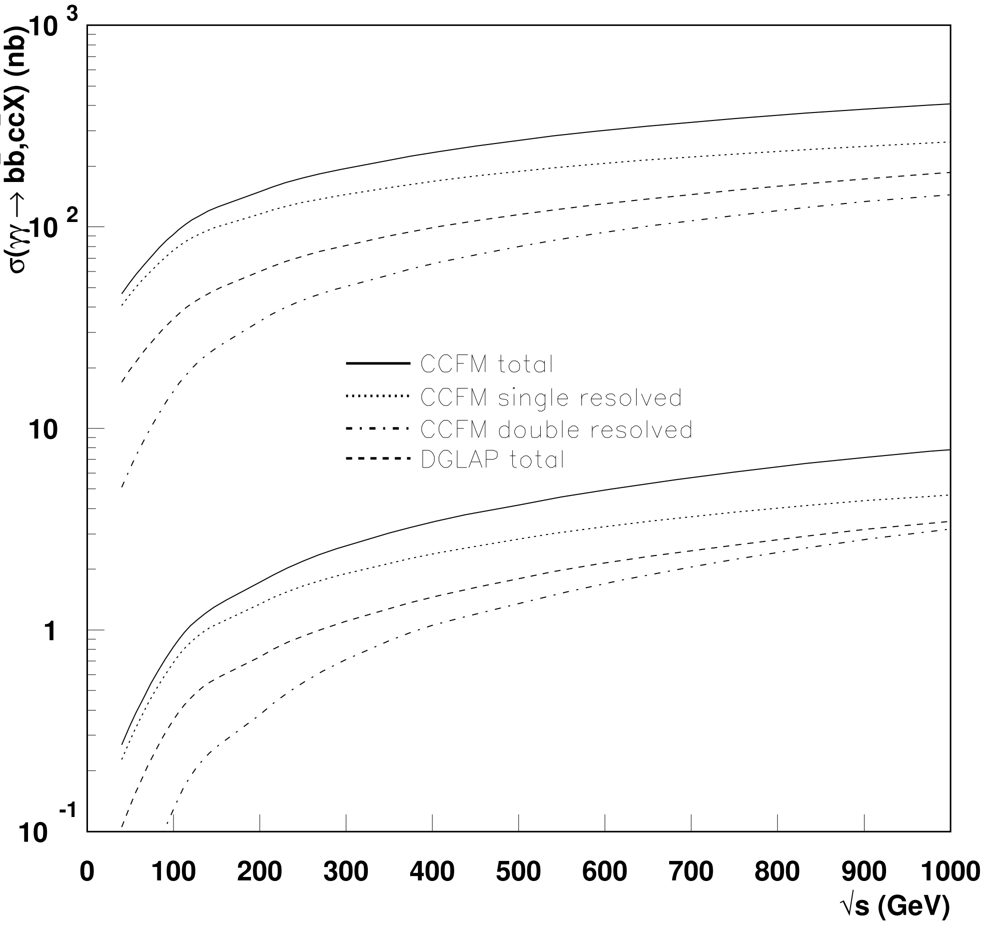

Figure 18: *Heavy quark cross section predictions for $\gamma\gamma$ collisions at TESLA energies. The masses $m_c = 1.5$ GeV and $m_b = 4.75$ GeV were used.*

with the default option (see Figure 11). Therefore, the cross sections were calculated also with these gluon densities to get an estimate of the error.

The strong coupling constant α_s is, despite its name, not a constant, but varies with the energy scale μ, according to (in a first approximation)

$$\alpha_s = \frac{12\pi}{(33 - 2 \cdot n_f)\ln(\frac{\mu^2}{\Lambda^2})}. \tag{18}$$

Here, n_f is the number of quark flavours with mass less than the energy scale μ, and Λ is a constant which has to be determined by experiments. The value of Λ also depends on the order that the process is calculated at. However, it is not clear how to compare the value of Λ used in the CCFM approach with the one used in NLO DGLAP, since the first order in the CCFM approach includes some second order diagrams in the DGLAP approach. The default value was chosen to be $\Lambda = 0.2$ GeV, which was also used in the evolution of the unintegrated gluon density, but $\Lambda = 0.34$ GeV (used in [42]) was also tested.

The energy scale μ is of the order of the typical momentum transfer, but the exact choice of scale should be such that the higher order contributions in the perturbative expansion of the cross section are minimal. The standard choice is $\mu^2 = m^2 + p_t^2$, where m is the heavy quark mass and p_t is the transverse momentum of the heavy quarks in the center of mass frame of the heavy quark system. To show the effect of the choice of μ, the scale $\mu^2 = 4m^2$ is also used here as a comparison.

The quark masses. Since the quarks are always confined in colorless hadrons, their masses cannot be measured directly. Instead, the masses must be extracted from hadron properties. However, this can be done in various ways depending on the exact definition of the quark masses, and different methods lead to slightly different results. Therefore, the heavy quark masses are varied such that 4.5 GeV $< m_b <$ 5 GeV and 1.3 GeV $< m_c <$ 1.7 GeV. This variation of the quark masses gives the largest uncertainty, and can therefore be used as an estimate of the total uncertainty, as seen in Figure 17, for example.

In Figure 19 is shown the cross sections for heavy quark production in e^+e^- collisions, calculated with different choices of Λ, μ^2 and unintegrated gluon densities. One can see that a change in Λ from $\Lambda = 0.2$ GeV to $\Lambda = 0.34$ GeV gives the largest variation of the cross sections, while changing μ^2 and the gluon density has a smaller effect. However, all these uncertainties are small compared to a change in the quark masses, see Figure 14.

9 Conclusions

The unintegrated gluon density for the photon was obtained with the full CCFM evolution for the first time. The CCFM evolved gluon density for the photon was used as input in the MC generator CASCADE, and cross sections for heavy quark production in e^+e^- collisions were calculated and compared to LEP data. Also, predictions for charm and beauty production in e^+e^- and $\gamma\gamma$ collisions at TESLA energies are given.

In e^+e^- collisions, the obtained cross sections were somewhat larger than NLO DGLAP predictions, but in good agreement with the charm data from LEP. The CCFM approach made a slight improvement compared to the standard collinear approach for the beauty cross sections. However, the improvement did not fully account for the discrepancy to the $b\bar{b}$ data.

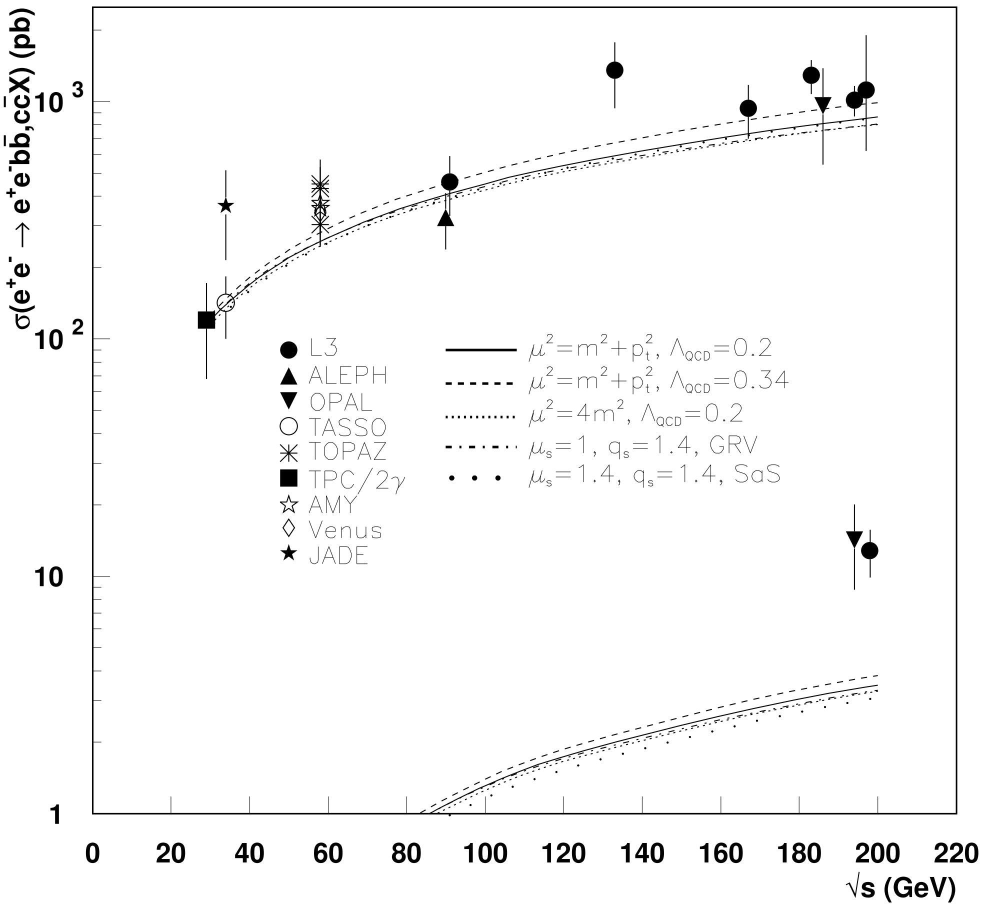

Figure 19: *The cross section dependence on Λ, μ^2 and different unintegrated gluon densities.*

10 Acknowledgements

This work was supported by INTAS grant 00-00679.

References

[1] D. Buskulic *et al.* (ALEPH Collaboration), *Phys. Lett.* **B 355** (1995) 595

[2] M. Acciarri *et al.* (L3 Collaboration), *Phys. Lett.* **B 453** (1999) 83

[3] M. Acciarri *et al.* (L3 Collaboration), *Phys. Lett.* **B 467** (1999) 137

[4] M. Acciarri *et al.* (L3 Collaboration), *Phys. Lett.* **B 503** (2001) 10

[5] M. Acciarri *et al.* (L3 Collaboration), *Phys. Lett.* **B 514** (2001) 19

[6] M. Acciarri *et al.* (L3 Collaboration), *Phys. Lett.* **B 536** (2002) 217

[7] The L3 Collaboration, L3 Note 2761

[8] The OPAL Collaboration, OPAL Physics Note PN455

[9] G. Abbiendi *et al.* (OPAL Collaboration), *Eur. Phys. J.* **C 16** (2000) 579

[10] G. Altarelli, T. Sjöstrand and F. Zwirner, Physics at LEP2, CERN 96-01 (1996)

[11] TESLA Technical Design Report, DESY 2001-11, TESLA Report 2001-23, TESLA-FEL 2001-05.

[12] P. Jankowski, M. Krawczyk and A. De Roeck, *Eur. Phys. J.* **C 24** (2002) 547

[13] C. Adloff *et al.* (H1 Collaboration), *Nucl. Phys.* **B 545** (1999) 21

[14] C. Adloff *et al.* (H1 Collaboration), *Phys. Lett.* **B 467** (1999) 156; erratum ibid.

[15] C. Adloff *et al.* (H1 Collaboration), *Phys. Lett.* **B 518** (2001) 331

[16] J. Breitweg *et al.* (ZEUS Collaboration), *Eur. Phys. J.* **C 6** (1999) 67

[17] J. Breitweg *et al.* (ZEUS Collaboration), *Eur. Phys. J.* **C 12** (2000) 35

[18] J. Breitweg *et al.* (ZEUS Collaboration), *Eur. Phys. J.* **C 18** (2001) 625

[19] F. Abe *et al.* (CDF Collaboration), *Phys. Rev. Lett.* **71** (1993) 500

[20] F. Abe *et al.* (CDF Collaboration), *Phys. Rev. Lett.* **71** (1993) 2396

[21] F. Abe *et al.* (CDF Collaboration), *Phys. Rev. Lett.* **75** (1995) 1451

[22] B. Abbot *et al.* (D0 Collaboration), *Phys. Lett.* **B 487** (2000) 264

[23] M. Cacciari and P. Nason, *Phys. Rev. Lett.* **89** (2002) 122003

[24] M. Cacciari, S. Frixione, M. L. Mangano, P. Nason and G. Ridolfi, "QCD analysis of first b cross section data at 1.96-TeV," arXiv:hep-ph/0312132.

[25] E. Gardi and M. Cacciari, "Perturbative and non-perturbative aspects of heavy-quark fragmentation," arXiv:hep-ph/0308235.

[26] H. Jung, Unintegrated parton densities applied to heavy quark production in the CCFM approach, in *Procedings of the Rinberg workshop on 'New trends in HERA physics', Rinberg Castle, Tegernsee, Germany* (2001), hep-ph/0109146

[27] H. Jung, Heavy quark production at the TEVATRON and HERA using k_t-factorization with CCFM evolution, Lund University, 2001, hep-ph/0110034, DESY 01-136

[28] L. Motyka and N. Timneanu, *Eur. Phys. J.* **C 27** (2003) 73

[29] M. Ciafaloni, *Nucl. Phys.* **B 296** (1988) 49

[30] S. Catani, F. Fiorani and G. Marchesini, *Phys. Lett.* **B 234** (1990) 339

[31] S. Catani, F. Fiorani and G. Marchesini, *Nucl. Phys.* **B 336** (1990) 18

[32] G. Marchesini, *Nucl. Phys.* **B 445** (1995) 49

[33] M. A. Kimber, A. D. Martin and M. G. Ryskin, *Phys. Rev.* **D 63** (2001) 114027

[34] N. Timneanu, J. Kwiecinski and L. Motyka, *Eur. Phys. J.* **C 23** (2002) 513

[35] K. Golec-Biernat and M. Wusthoff, *Phys. Rev.* **D 59** (1999) 014017

[36] R. Brock *et al.* (CTEQ Collaboration), FERMILAB-PUB-94-316

[37] S. Catani, M. Ciafaloni and F. Hautmann, *Nucl. Phys.* **B 366** (1991) 135

[38] J. Collins and R. Ellis, *Nucl. Phys.* **B 360** (1991) 3

[39] L. Gribov, E. Levin and M. Ryskin, *Phys. Rept.* **100** (1983) 1

[40] E.M. Levin, M.G. Ryskin, Y.M. Shabelski and A.G. Shuvaev, *Sov. J. Nucl. Phys.* **53** (1991) 657

[41] B. Andersson *et al.* (Small x Collaboration), *Eur. Phys. J.* **C 25** (2002) 77

[42] M. Drees *et al.*, *Phys. Lett.* **B 306** (1993) 371

[43] E. Boos, M. Sachwitz, H. J. Schreiber and S. Shichanin, DESY-96-007 *3rd Workshop on Physics and Experiments with E+ E- Linear Colliders (LCWS95), LCWS95: Department Physics: KEK, National Lab for High Energy Physics: 1-1 Oho, Tsukuba-shi: Ibaraki-ken, 305 Japan, 8-12 Sep 1995, Iwate, Japan*

[44] V. Gribov and L. Lipatov, *Sov. J. Nucl. Phys.* **15** (1972) 438 and 675

[45] L. Lipatov, *Sov. J. Nucl. Phys.* **20** (1975) 94

[46] G. Altarelli and G. Parisi, *Nucl. Phys.* **B 126** (1977) 298

[47] Y. Dokshitzer, *Sov. Phys. JETP* **46** (1977) 641

[48] E. Kuraev, L. Lipatov and V. Fadin, *Sov. Phys. JETP* **44** (1976) 443

[49] E. Kuraev, L. Lipatov and V. Fadin, *Sov. Phys. JETP* **45** (1977) 199

[50] Y. Balinsky and L. Lipatov, *Sov. J. Nucl. Phys.* **28** (1978) 822

[51] H. Jung, *Comp. Phys. Comm.* **143** (2002) 100

[52] T. Sjöstrand, *Comp. Phys. Comm.* **82** (1994) 74

[53] H. Plothow-Besch, 'The Parton Distribution Function Library', *Int. J. Mod. Phys.* **A 10** (1995) 2901

[54] A. I. Shoshi, F. D. Steffen, H. G. Dosch and H. J. Pirner, *Phys. Rev.* **D 66** (2002) 094019

[55] The CERN Program Library

[56] W. H. Press *et al.*, *Numerical recepies in Fortran, second edition* (Cambridge University Press, New York, 1992)

[57] M. Glück, E. Reya and A. Vogt, *Phys. Rev.* **D 45** (1992) 3986

[58] G. Ingelman, A. Edin and J. Rathsman, *Comp. Phys. Comm.* **101** (1997) 108

[59] H. Jung and G. P. Salam, *Eur. Phys. J.* **C 19** (2001) 351

[60] B. R. Webber, *Nucl. Phys. Proc. Suppl.* **18C** (1991) 38.

[61] G. Marchesini and B. R. Webber, *Nucl. Phys.* **B 386** (1992) 215.

[62] A. Gawron and J. Kwiecinski, *Acta Phys. Polon.* **B 34** (2003) 133

[63] S. P. Baranov *et al.*, *Eur. Phys. J.* **C 24** (2002) 425

[64] G. A. Schuler and T. Sjöstrand, *Phys. Lett.* **B 276** (1996) 193